Chem. Mater. **2008,** *20,* 1183–1190

Physical and Optical Properties of Inverse Opal CeO_2 Photonic Crystals[†]

Geoffrey I. N. Waterhouse,* James B. Metson, Hicham Idriss, and Dongxiao Sun-Waterhouse

Department of Chemistry, University of Auckland, Private Bag 90219, Auckland, New Zealand

Received October 18, 2007. Revised Manuscript Received December 19, 2007

Inverse opal ceria (CeO_2) films and powders, exhibiting three-dimensional ordered macroporous (3DOM) structures and a photonic band gap (PBG) in the visible region, were successfully fabricated using the colloidal crystal template approach. Colloidal crystals templates, comprising polymethylmethacrylate (PMMA) spheres of diameter ~325 nm arranged on a face-centered cubic (fcc) lattice, were prepared by self-assembly from aqueous colloidal suspensions of PMMA spheres. After drying, the interstitial spaces in the PMMA colloidal crystals were filled with a ceria sol–gel precursor, and then the resulting structure calcined at 400 °C to remove the polymer template. The ceria inverse opals obtained were characterized by SEM, XRD, BET, porosity, and UV–vis transmittance measurements and showed fcc ordering of macropores (diameter around 240 nm) within a CeO_2 nanocrystal matrix. The CeO_2 volume fraction in the inverse opals was 17–18 vol %, and its surface area was 51 $m^2\ g^{-1}$. Both the PMMA colloidal crystals and CeO_2 inverse opals behaved as 3-dimensional photonic crystals, with PBGs at 877 and 485 nm, respectively. Filling the macropores of the CeO_2 inverse opal with solvent caused a redshift in the position of the PBG, with the magnitude of the shift being directly proportional to the refractive index of the solvent. Refractive index sensing with a sensitivity of $n = 0.001$ or better is achievable using inverse opal CeO_2 thin films. Inverse opal CeO_2 powders showed improved thermal stability at 800 °C compared to non-networked ceria nanoparticles of similar initial crystallite size and surface area, suggesting that inverse opal architectures may be useful in applications where retention of large surface area during high temperature operation is important (e.g., heterogeneous catalysis).

Introduction

Photonic crystals are highly ordered structures with a periodically modulated refractive index, with periods typically on the length scale of optical wavelengths (380–750 nm). Periodicity may exist in one, two, or three dimensions and affects the propagation of electromagnetic waves in the material because of the Bragg diffraction on lattice planes. The result is a photonic band gap (PBG or stop band),[1–7] a band of frequencies for which light propagation in the photonic crystal is forbidden (i.e., periodicity causes partial or total suppression of photon density of states (DOS) for certain frequencies of electromagnetic radiation). A complete photonic band gap occurs when a range of frequencies is forbidden for every state of polarization and propagation direction.[1–7] Because of their ability to confine, control, and manipulate photons in up to 3D, a wide variety of applications are envisioned for PBG materials (including optical, electro-optical and quantum electronic devices). Before their full potential can be realized, improved and inexpensive methods for the fabrication of highly ordered 3D photonic crystals must be developed.

Photonic crystals have traditionally been fabricated using either top-down (microlithography) or bottom-up (self-assembly) approaches. Fabrication of 1D or 2D photonic crystals using microlithography is relatively straightforward, but technical challenges and obstacles exist to the fabrication of 3D lattices with long-range order.[8–10] For this reason, researchers generally prefer the bottom up approach, and in particular the colloidal crystal template method,[11–29] for the

---

[†] Part of the "Templated Materials Special Issue".

* Corresponding author. Fax: 64 9 3737422. Tel: 64 9 3737599, ext. 87212. E-mail: g.waterhouse@auckland.ac.nz.

(1) Joannopoulos, J. D.; Meade, R. D.; Winn, J. N. *Photonic Crystals: Molding the Flow of Light*; Princeton University Press: Princeton, NJ, 1995.
(2) Yablonovitch, E. *Phys. Rev. Lett.* **1987**, *58*, 2059–2062.
(3) John, S. *Phys. Rev. Lett.* **1987**, *58*, 2486–2489.
(4) Joannopoulos, J. D.; Villeneuve, P. R.; Fan, S. *Nature* **1997**, *386*, 143–149.
(5) Busch, K.; John, S. *Phys. Rev. E* **1998**, *58*, 3896–3908.
(6) Biswas, R.; Sigalas, M. M.; Subramania, G.; Ho, K.-M. *Phys. Rev. B* **1998**, *57*, 3701–3705.
(7) Biswas, R.; Sigalas, M. M.; Subramania, G.; Soukoulis, C. M.; Ho, K.-M. *Phys. Rev. B* **2000**, *61*, 4549–4553.
(8) Yablonovitch, E.; Gmitter, T. J.; Leung, K. M. *Phys. Rev. Lett.* **1991**, *67*, 2295–2298.
(9) Noda, S.; Tomoda, K.; Yamamoto, N.; Chutinan, A. *Science* **2000**, *289*, 604–606.
(10) Qi, M.; Lidorikis, E.; Rakich, P. T.; Johnson, S. G.; Joannopoulos, J. D.; Ippen, E. P.; Smith, H. I. *Nature* **2004**, *429*, 538–542.
(11) García-Santamaría, F.; Galisteo-López, J. F.; Braun, P. V.; López, C. *Phys. Rev. B* **2005**, *71*, 195112.
(12) Zhou, Z.; Zhao, X. S. *Langmuir* **2004**, *20*, 1524–1526.
(13) Zhou, Z.; Zhao, X. S. *Langmuir* **2005**, *21*, 4717–4723.
(14) Xia, Y.; Gates, B.; Yin, Y.; Lu, Y. *Adv. Mater.* **2000**, *12*, 693–713.
(15) Stein, A.; Schroden, R. C. *Curr. Opin. Solid State Mater. Sci.* **2001**, *5*, 553–564.
(16) Blanco, A.; Chomski, E.; Grabtchak, S.; Ibisate, M.; John, S.; Leonard, S. W.; Lopez, C.; Meseguer, F.; Miguez, H.; Mondia, J. P.; Ozin, G. A.; Toader, O.; van Driel, H. M. *Nature* **2000**, *405*, 437–440.
(17) Míguez, H.; Chomski, E.; García-Santamaría, F.; Ibisate, M.; John, S.; López, C.; Meseguer, F.; Mondia, J. P.; Ozin, G. A.; Toader, O.; van Driel, H. M. *Adv. Mater.* **2001**, *13*, 1634–1637.

10.1021/cm703005g CCC: $40.75

fabrication of 3D photonic crystal structures. The colloidal crystal template method comprises three common steps. In the first step, a 3D colloidal crystal template (i.e., a synthetic opal) is prepared by the self-assembly of monodisperse silica or polymer (polystyrene or PMMA) spheres on a face-centered cubic (fcc) lattice.[11–29] The resulting colloidal crystal is typically 74% solid and 26% air by volume. A photonic band gap exists in the [111] direction for fcc arrangements of spheres[5–7] and will occur in the visible region for silica or polymer spheres with diameters between 180 and 350 nm. In the second step, the interstitial space in the colloidal crystal is filled with a dielectric material, using sol–gel, chemical vapor deposition (CVD), electrocrystallization, or nanoparticle infiltration methods.[14–29] Finally, the colloidal crystal template is removed by wet chemical etching (for SiO_2 or polymer spheres) or calcination (for polymer spheres only). The resulting inverted replica of the original colloidal crystal, commonly termed an inverse opal, comprises a 3D fcc array of air spheres (macropores) in a dielectric matrix.[14–29] Inverse opals of appropriate spatial periodicity will exhibit a PBG for diffraction from (111) planes in the visible region. The position of the PBG and hence observed reflected color depends on the periodicity in the [111] direction, the refractive index and volume fraction (typically 10–26 vol %) of the dielectric wall material, the refractive index of the medium filling the macropores (typically air) and the incident angle of light with respect to the (111) surface normal. If the refractive index contrast between the wall and pore materials is sufficiently large ($n_{wall}/n_{air} > 2.9$), inverse opal materials may exhibit a complete photonic band gap. Silicon and germanium inverse opals with a complete 3D PBG in the near-IR region have already been demonstrated.[16–18] Optical applications for these and other inverse opal photonic crystal materials are presently being explored. The cracking of colloidal crystal templates on drying, which introduces structural defects that are propagated in the inverse opal replicas, remains the chief technical barrier to the commercialization of complete PBG inverse opal materials and devices.

Aside from their fascinating optical properties, inverse opal materials are attracting attention because of their inherent structural and physical properties, such as high surface area and 3D ordered macroporous structure (3DOM), which makes them desirable for many applications including dye-sensitized solar cells,[22–24] sensors,[25–27] microfluidic devices,[28] separation,[28] and catalysis.[29] In this regard, the fabrication of inverse opal ceria (CeO_2) warrants investigation, because CeO_2 and ceria-based materials are utilized in many areas of technological importance. CeO_2 crystallizes with the fluorite structure ($Fm3m$, $Z = 4$, $a = 5.4087–5.411$ Å)[30] and is a key component of automotive three-way exhaust catalysts because of its high oxygen storage capacity (OSC),[31] which derives from its ability to undergo rapid reversible redox cycles of the type $CeO_2 \leftrightarrow CeO_{2-x} + {}^{x}/_{2}O_2$ in response to changes in oxygen availability. Ceria-supported metal nanoparticle catalysts are also active for methane reforming,[32] ethanol reforming,[33–36] CO oxidation,[37] and the water gas shift reaction.[38,39] The performance of ceria in most applications depends strongly on the shape and size of the CeO_2 particles. For example, nanocrystalline ceria increases the activity of gold nanoparticles for CO oxidation by 2 orders of magnitude compared to micron sized ceria supports.[37] Accordingly considerable research effort continues to be directed toward the synthesis of CeO_2 powders with improved physicochemical properties,[31–44] and in particular small crystallite size, large surface area, large OSC, and high sintering resistance. To date, only one study examining the fabrication and physicochemical properties of inverse opal CeO_2 has appeared in the literature,[20] justifying further research in this area. No information about the optical properties of inverse opal ceria is presently available. CeO_2 is expected to be useful for photonic crystal optical applications as it has a high refractive index ($n = 2.4$) and good transparency in the visible and near-IR region.[45]

The present paper describes the fabrication of inverse opal CeO_2 films and powders, using sol–gel procedures and PMMA colloidal crystals as templates. Through detailed

---

(18) Tétreault, N.; Míguez, H.; Ozin, G. A. *Adv. Mater.* **2004**, *16*, 1471–1476.

(19) Schroden, R. C.; Al-Daous, M.; Blanford, C. F.; Stein, A. *Chem. Mater.* **2002**, *14*, 3305–3315.

(20) Wu, Q. Z.; Shen, Y.; Liao, J. F.; Li, Y. G. *Mater. Lett.* **2004**, *58*, 2688–2691.

(21) Waterhouse, G. I. N.; Waterland, M. W. *Polyhedron* **2007**, *26*, 356–368.

(22) Huisman, C. L.; Schoonman, J.; Goossens, A. *Sol. Energy Mater. Sol. Cells* **2005**, *85*, 115–124.

(23) Halaoui, L. I.; Abrams, N. M.; Mallouk, T. E. *J. Phys. Chem. B* **2005**, *109*, 6334–6342.

(24) Rodriguez, I.; Atienzar, P.; Ramiro-Manzano, F.; Meseguer, F.; Corma, A.; Garcia, H. *Photonics Nanostruct.* **2005**, *3*, 148–154.

(25) Scott, R. W. J.; Yang, S. M.; Chabanis, G.; Coombs, N.; Williams, D. E.; Ozin, G. A. *Adv. Mater.* **2001**, *13*, 1468–1472.

(26) Prasad, T.; Mittleman, D. M.; Colvin, V. L. *Opt. Mater.* **2006**, *29*, 56–59.

(27) Kuo, C.-Y.; Lu, S.-Y.; Chen, S.; Bernards, M.; Jiang, S. *Sens. Actuators, B* **2007**, *124*, 452–458.

(28) Kuo, C.-W.; Shiu, J.-Y.; Kung, H. W.; Chen, P. *J. Chromatogr., A* **2007**, *1162*, 175–179.

(29) Ren, M.; Ravikrishna, R.; Valsaraj, K. T. *Environ. Sci. Technol.* **2006**, *40*, 7029–7033.

(30) Mogensen, M.; Sammes, N. M.; Tompsett, G. A. *Solid State Ionics* **2000**, *129*, 63–94.

(31) Kăspar, J.; Fornasiero, P.; Graziani, M. *Catal. Today* **1999**, *50*, 285–298.

(32) Laosiripojana, N.; Assabumrungrat, S. *Appl. Catal., B* **2005**, *60*, 107–116.

(33) Hsiao, W.-I.; Lin, Y.-S.; Chen, Y.-C.; Lee, C.-S. *Chem. Phys. Lett.* **2007**, *441*, 294–299.

(34) Erd″ohelyi, A.; Raskŏ, J.; Kecskés, T.; Tŏth, M.; Dömök, M.; Baán, K. *Catal. Today,* **2006**, *116*, 367–376.

(35) Idriss, H. *Platinum Met. Rev.* **2004**, *48*, 105–115.

(36) Sheng, P.-Y.; Bowmaker, G. A.; Idriss, H. *Appl. Catal., A* **2004**, *261*, 171–181.

(37) Carrettin, S.; Concepción, P.; Corma, A.; López Nieto, J. M.; Puntes, V. F. *Angew. Chem., Int. Ed.* **2004**, *43*, 2538–2540.

(38) Jacobs, G.; Crawford, A.; Williams, L.; Patterson, P. M.; Davis, B. H. *Appl. Catal., A* **2004**, *267*, 27–33.

(39) Fu, Q.; Kudriavtseva, S.; Saltsburg, H.; Flytzani-Stephanopoulos, M. *Chem. Eng. J.* **2003**, *93*, 41–53.

(40) Zhang, F.; Jin, Q.; Chan, S.-W. *J. Appl. Phys.* **2004**, *95*, 4319–4326.

(41) Wu, L.; Weismann, H. J.; Moodenbaugh, A. R.; Klie, R. F.; Zhu, Y.; Welch, D. O.; Suenaga, M. *Phys. Rev. B* **2004**, *69*, 125415.

(42) Bumajdad, A.; Zaki, M. I.; Eastoe, J.; Pasupulety, L. *Langmuir* **2004**, *20*, 11223–11233.

(43) Laberty-Robert, C.; Long, J. W.; Lucas, E. M.; Pettigrew, K. A.; Stroud, R. M.; Doescher, M. S.; Rolison, D. R. *Chem. Mater.* **2006**, *18*, 50–58.

(44) Sun, C.; Li, H.; Chen, L. *J. Phys. Chem. Solids* **2007**, *68*, 1785–1790.

(45) Narasimha Rao, K.; Shivlingappa, L.; Mohan, S. *Mater. Sci. Eng.* **2003**, *B98*, 38–44.

characterization of the physical, structural and optical properties of ceria inverse opals, we hoped to ascertain the general suitability of this material for advanced optical and catalytic applications.

Experimental Section

Materials. Methyl methacrylate (99%), 2,2′-azobis(2-methylpropionamidine) dihydrochloride (97%), concentrated HCl (37% in water), $Ce(NO_3)_3.6H_2O$ (99%), citric acid (99%), urea (98%), ammonia (28% in water), CeO_2 powder (99.9%, $<5\ \mu m$), and all organic solvents were obtained from Aldrich and used without further purification.

Synthesis of Polymethylmethacrylate (PMMA) Spheres. Monodisperse PMMA spheres with a diameter of approximately 325 nm (as determined by SEM) were prepared by the free-radical-initiated emulsion polymerization of methyl methacrylate.[19,21] Briefly, methyl methacrylate (400 mL) and milli Q water (1.6 L) were added to a 3 L round-bottomed flask. Nitrogen gas was then slowly bubbled through the resulting two-phase system and vigorous mechanical stirring of the emulsion commenced. The emulsion was then heated to 70 °C, whereupon 2,2′-azobis(2-methylpropionamidine) dihydrochloride (1.5 g) was added and polymerization of the methyl methacrylate commenced. The temperature of the reaction mixture increased initially on introduction of the initiator, but then stabilized after approximately 30 min. After stabilization, the reaction mixture was maintained at the initial temperature of 70 °C for 2 h. Heating was then discontinued, and the reaction mixture allowed to cool to room temperature over 3–4 h under a nitrogen purge. The resulting colloidal suspensions of PMMA spheres (approximately 20 wt % PMMA in water) were filtered through a glass wool plug to remove any large agglomerates and stored in PET plastic bottles for later use.

Colloidal Crystal Template Preparation. Colloidal crystal templates comprising PMMA spheres arranged on a face-centered cubic (fcc) lattice were fabricated using two methods.

(1) Centrifugation. PMMA colloidal suspensions were loaded into 50 mL plastic falcon tubes, then centrifuged at 1500 rpm (rcf 369) for 24 h. The supernatant was then carefully removed by decantation, and the colloidal crystals left to dry in air at 25 °C for 1–2 weeks.

(2) A flow-controlled vertical deposition method.[12,13] This method was used to deposit thin PMMA colloidal crystals on glass microscope slides for UV–vis transmittance measurements. Briefly, a colloidal suspension of PMMA spheres (100 mL, 4 wt % PMMA in H_2O) was prepared and poured into a glass beaker. Several glass microscope slides were immersed vertically in the colloidal suspension, after which a peristaltic pump was used to slowly remove the colloidal suspension (pump rate about 0.2 mL min^{-1}). As the liquid level in the beaker decreased a thin PMMA colloidal crystal film of approximately 10 μm thickness deposited on the glass slides.

Ceria Inverse Opal Preparation. CeO_2 inverse opals were prepared by filling the voids in PMMA colloidal crystal templates with a ceria sol–gel precursor, then calcining the resulting CeO_2/PMMA composite to remove the PMMA template. For the preparation of inverse opal CeO_2 powders, the filling of the voids in the colloidal crystal template was achieved using a vacuum-assisted infiltration method.[15,19–21] Briefly, PMMA colloidal crystals (5 g) prepared by centrifugation were lightly crushed with a metal spatula to give fractured pieces of size <2 mm, which were then deposited in a thin layer on filter paper in a large Büchner funnel. With a strong vacuum applied to the Büchner funnel, a ceria sol–gel precursor solution containing $Ce(NO_3)_3\cdot 6H_2O$ (2.17 g) and citric acid (1.05 g) in ethanol (10 mL) was applied dropwise over the surface of the PMMA layer. Infiltrated samples were then left to hydrolyze and gel in air at 25 °C for 24 h. The resulting CeO_2/PMMA composites were then calcined using the following protocol; samples were ramped in air from 25 to 300 °C at 2 °C min^{-1}; held at 300 °C for 2 h; ramped from 300 to 400 °C at 2 °C min^{-1}; held at 400 °C for 2 h; and then finally allowed to cool to room temperature over 3–4 h. The inverse opal CeO_2 powders obtained exhibited visible opalescence under incident white light.

For UV–vis transmittance measurements, inverse opal CeO_2 films were fabricated using PMMA colloidal crystals grown on glass microscope slides. PMMA templates were infiltrated by carefully placing a few drops of the ceria sol–gel precursor solution, diluted 10-fold in ethanol, on one edge of the colloidal crystal. Capillary forces quickly drew the sol–gel mixture into the voids in the PMMA template. The infiltrated crystal was then aged for 24 h under ambient conditions, and then calcined in accordance with procedure described above.

Ceria Nanoparticle Preparation. Ceria nanoparticles were prepared from $Ce(NO_3)_3\cdot 6H_2O$ using two common literature procedures,[36,38] and used as reference materials. A first preparation of ceria nanoparticles (denoted as Prep 1 CeO_2 nanoparticles in the text below) was obtained by the urea gelation precipitation (UGP) method.[38] $Ce(NO_3)_3\cdot 6H_2O$ (0.175 M) and urea (4 M) were dissolved in 1 L of milli Q water at room temperature. Under vigorous stirring, concentrated aqueous NH_3 (30 mL, 28 wt %) was added dropwise at a rate of approximately 1 mL min^{-1}. After addition of all the NH_3, the resulting solution was brought to the boil and maintained at boiling for 8 h. Milli Q water was added periodically to maintain a constant volume of 1 L. After 8 h, the boiling was discontinued and the precipitate formed collected by vacuum filtration on a Büchner funnel. The precipitate was washed repeatedly with milli Q water and then dried in air at 100 °C for 12 h. Calcination at 400 °C for 2 h yielded CeO_2 nanoparticles of average diameter 12.9 nm and specific surface area 74.5 $m^2\ g^{-1}$. A second preparation of CeO_2 nanoparticles (denoted as Prep 2 CeO_2 nanoparticles in the text below) was obtained by the slow dropwise addition of concentrated aqueous NH_3 (35 mL, 28 wt %) to a vigorously stirred solution of 0.1 M $Ce(NO_3)_3\cdot 6H_2O$ (400 mL) at 100 °C.[36] The precipitate obtained at pH 8–9 was aged for 1 h at 100 °C in the mother liquour and then collected by vacuum filtration on a Büchner funnel. After repeated washing with milli Q water the precipitate was dried at 100 °C for 12 h. Calcination at 400 °C for 2 h yielded CeO_2 nanoparticles of average diameter 13.5 nm and specific surface area 32.9 $m^2\ g^{-1}$.

Characterization. Specimen morphologies were examined using a Philips XL-30 field-emission gun scanning electron microscope (FEGSEM). All micrographs were collected at an electron gun accelerating voltage of 5 kV. Specimens were mounted on black carbon tape and platinum sputter coated for analysis.

Powder X-ray diffraction patterns were collected using a Philips PW-1130 diffractometer, equipped with a Cu anode X-ray tube and a curved graphite filter monochromator. XRD data was collected from $2\theta = 2$–$100°$ (0.02°, 2° min^{-1}) using Cu Kα X-rays ($\lambda = 1.5418$ Å). The ceria lattice parameter (a) was obtained from the powder XRD data by plotting the lattice parameter $a = d_{hkl}\sqrt{h^2 + k^2 + l^2}$ calculated for each (hkl) reflection against $\cos^2 \theta$. Extrapolation to $\cos^2 \theta = 0$ yields the lattice parameter to within 0.005% accuracy.[40] Ceria crystallite sizes (L) were determined from the powder XRD data using the line width of the ceria (111) reflection and the Scherrer equation.

N_2 adsorption isotherms were determined at liquid nitrogen temperature (−195 °C) using a Micromeritics Tristar 3000 instrument. Specific surfaces areas were calculated from the N_2 adsorption

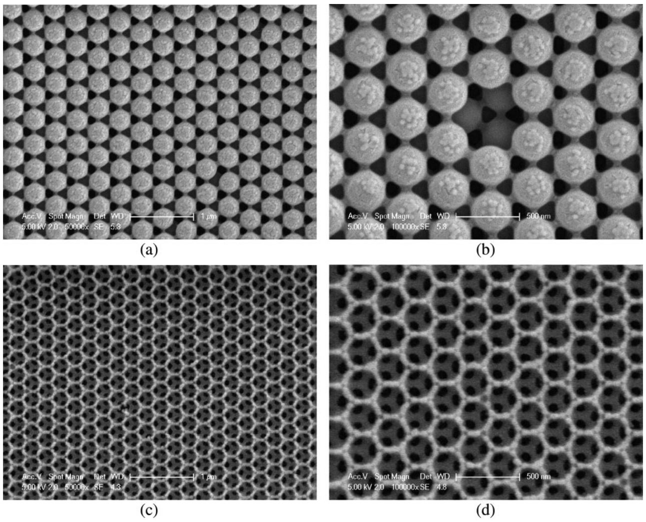

Figure 1. SEM micrographs of (a, b) a PMMA colloidal crystal thin film and (c, d) an inverse opal CeO_2 thin film. Micrographs on the left were taken at 50 000× (scale bar = 1 μm), those on the right at 100 000× magnification (scale bar = 500 nm). Both the PMMA colloidal crystal and inverse opal ceria films show a fcc arrangement of spheres, with their fcc (111) planes parallel to the underlying glass substrate.

data according to the Brunauer–Emmett–Teller (BET) method. Cumulative pore volumes and pore diameters were calculated from the adsorption isotherms by the Barrett–Joyner–Halenda (BJH) method. Samples were degassed at 200 °C for 2 h under a dry N_2 gas purge prior to the N_2 adsorption measurements.

UV–vis transmittance spectra were recorded over the range 200–1000 nm on a Shimadzu U-3101PC spectrophotometer, equipped with a custom-built sample holder for angle-resolved UV–vis transmittance measurements.

Results and Discussion

SEM Characterization of the PMMA Colloidal Crystal Templates (Synthetic Opals) and CeO_2 Inverse Opals. The PMMA colloidal crystal templates fabricated in this study exhibited strong opalescence under incident white light, visible evidence of their long-range 3D order. Figure 1a and b show SEM micrographs taken from a PMMA colloidal crystal film deposited on a glass microscope slide. The images show a fcc arrangement of monodisperse PMMA spheres with diameter ~ 325 nm, whose (111) planes are oriented parallel to the underlying glass substrate. Figure 1b shows the necking of the PMMA spheres to their nearest neighbors and also the arrangement of spheres in the underlying layer. The center-to-center distance between spheres on the individual (111) planes, measured directly from the SEM images, is approximately 395–400 nm. SEM micrographs taken from PMMA colloidal crystal powders showed a similar fcc ordering of spheres (not shown).

CeO_2 inverse opal films displayed an indigo-blue opalescence under white light illumination, confirming the success of the colloidal crystal templating procedure. Images c and d in Figure 1 show SEM micrographs for a ceria inverse opal thin film. The film exhibits a 3D ordered macroporous structure comprising interconnected macropores arranged on a fcc lattice. The center-to-center distance between the macropores on the (111) planes is ~240 nm, and the ceria fraction of the inverse opals is around 17–18 vol % (these values are estimated directly from the micrographs). The dark areas within the macropores result from the necking of PMMA spheres in the colloidal crystal template (cf. Figure 1b). Removal of the polymer template by calcination caused a large shrinkage of the fcc lattice. This can be seen by directly comparing Figure 1b with Figure 1d (images taken at the same magnification). In the case of the inverse opal, the center-to-center distance (*D*) between neighboring macropores on the individual (111) planes was approximately 40% smaller than the corresponding distance between spheres in the colloidal crystal template. The shrinkage likely originates from thermal decomposition of the citric acid chelator during the calcination step. Comparable shrinkage was reported by Wu et al. for 3DOM CeO_2 powders prepared from polystyrene colloidal crystal templates.[20]

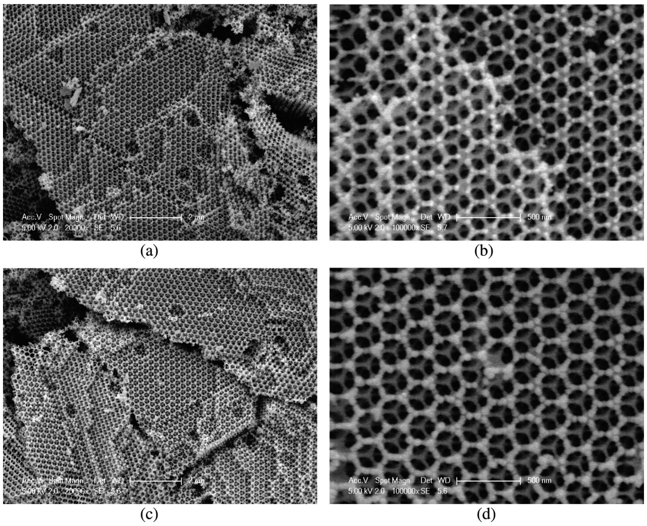

Figure 2. SEM micrographs of inverse opal CeO_2 powders: (a, b) as-prepared inverse opal CeO_2 powder and (c, d) inverse opal CeO_2 powder after calcination at 800 °C for 4 h. Micrographs on the left were taken at 20 000× (scale bar = 2 μm), those on the right at 100 000× magnification (scale bar = 500 nm). The 3DOM structure of the ceria inverse opal remains after calcination at 800 °C.

SEM images taken from the as-prepared inverse opal CeO_2 powders (images a and b in Figure 2) were similar to the films in terms of macropore diameters. Well-defined steps, facets, and terrace structures are evident in the micrographs, and result from the intentional crushing of the PMMA colloidal crystal prior to infiltration with the ceria sol–gel precursor. Note that fracture occurred along well-defined crystallographic planes in the fcc lattice. The ceria volume fraction in the powders is slightly lower than that observed for the films (cf. Figure 2b and Figure 1d, respectively), which relates to the different methods used to infiltrate the respective PMMA colloidal crystal templates with the ceria sol–gel precursor (see experimental section).

Most applications using ceria require high-temperature operation (up to 900 °C).[30–39] Therefore, it is important to investigate the thermal stability of inverse opal ceria. Images c and d in Figure 2 present SEM micrographs of a ceria inverse opal particle after calcination at 800 °C for 4 h. Remarkably, the macroporous 3D structure of the inverse opal was largely unaffected by the high temperature treatment. The effect of calcination on the physical and structural

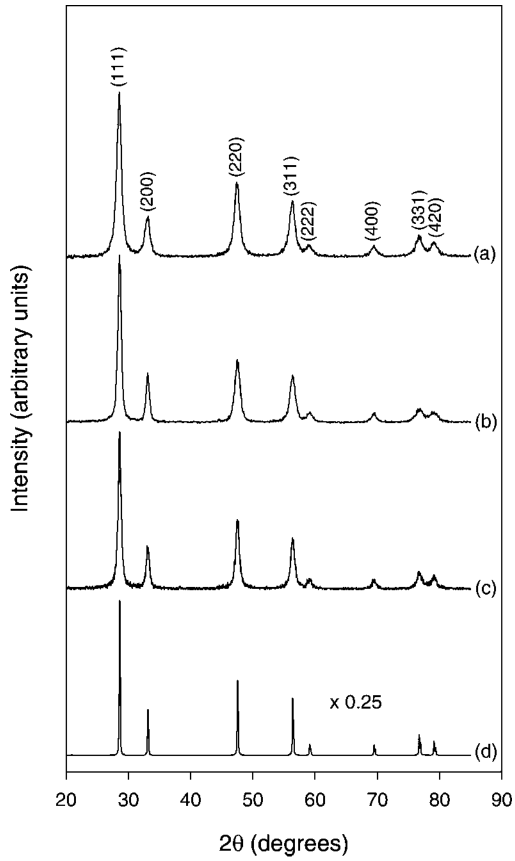

Figure 3. X-ray powder diffractograms for (a) as-prepared inverse opal CeO_2 powder; (b) Prep 1 CeO_2 nanoparticles; (c) Prep 2 CeO_2 nanoparticles; and (d) a micrometer-sized CeO_2 powder. The line-broadening observed for the inverse opal CeO_2 powder and nanoparticle preparations results from size-induced relaxation effects and an increase in the lattice parameter.

properties of the ceria inverse opal is examined in further detail below.

Structural Characterization of the CeO_2 Inverse Opals. The structural form of ceria in the walls of the inverse opal is of interest, since for most technological applications ceria nanoparticles are preferred.[30–39] XRD patterns taken from the as-prepared CeO_2 inverse opal, ceria nanoparticles prepared using two common literature routes and a micron sized ceria powder are shown in Figure 3. The diffractograms all contain peaks characteristic for cubic CeO_2,[32–44] although in the case of the ceria inverse opal (Figure 3a) and nanoparticle preparations (plots b and c in Figure 3), the peaks are broader and shifted slightly to lower 2θ values compared to the micron sized powder (Figure 3d). The line broadening and 2θ shifts observed for nanometer-sized ceria particles result from size-induced lattice relaxation effects and an increase in the lattice parameter.[40,41]

Unit-cell parameters and average crystallite sizes extracted from the diffractograms of Figure 3, as well as specific surface areas and porosity data collected for each sample, are summarized in Table 1. Corresponding data obtained after the calcination of each sample at 800 °C for 4 h is also provided, and is discussed below. Results show that the as-prepared CeO_2 inverse opal comprises ceria nanocrystals with average diameter 9.4 nm and a lattice parameter of 5.419 Å (Table 1). The lattice parameter was approximately 0.2% larger than that determined for the micron sized ceria powder (5.410 Å), evidence of size-induced lattice expansion. Bulk ceria is reported to have a lattice parameter $a = 5.4087–5.411$ Å,[32–44] in excellent agreement with the value of 5.410 Å determined here. The specific surface area of the ceria inverse opal was 51.0 $m^2\ g^{-1}$ and the cumulative pore volume 0.124 $cm^3\ g^{-1}$. The ceria nanoparticle preparations (Prep 1 and 2) and inverse opal exhibited comparable initial ceria crystallite size and lattice parameters, although significant differences were found between the samples in terms of their specific surface area and porosity (Table 1). Preparation method thus strongly influences the physicochemical properties of nanocrystalline ceria, in agreement with previous literature reports.[32–44]

Calcination at 800 °C increased the average size of the ceria crystallites in the walls of the inverse opal from 9.4 to 38.3 nm, and caused a concomitant decrease in the lattice parameter, specific surface area and cumulative pore volume (Table 1). By SEM, no visible differences were seen between samples before and after calcination (Figure 2). Thus, the ceria crystallite size, lattice parameter, BET surface area, and cumulative pore volume have little relationship to the geometry of the inverse opal macropores. High temperature treatment had a similarly adverse affect on the physical properties of two ceria nanoparticle preparations, especially preparation 2, which suffered a catastrophic 93% loss of surface area after calcination at 800 °C (Table 1). Retention of a large surface area during high temperature operation is a key requirement of ceria materials for most applications.[30–39] Inverse opal ceria appears to be preferable to non-networked ceria nanoparticles in this regard, because the inverse opal retains a 3DOM structure at high temperature (images c and d in Figure 2) that limits the extent of ceria densification.

Optical Properties of the PMMA Colloidal Crystals and CeO_2 Inverse Opals. The position of photonic band gaps (PBGs or stop bands) in fcc photonic crystals can be estimated using a modified form of Bragg's law which takes into account refraction of light in the periodic structure and the incident angle of the incoming light[11–29]

$$\lambda_{\max} = \frac{2d_{hkl}}{m}\sqrt{{n_{\mathrm{avg}}}^2 - \sin^2\theta} \qquad (1)$$

where $\lambda_{\max}$ is the wavelength of the reflectance peak maximum (i.e., the position of the PBG), d_{hkl} is the interplanar spacing between (hkl) planes, m is the order of the Bragg diffraction, n_{avg} is the average refractive index of the photonic structure, and θ is the angle between the incident light and the surface normal of the sample. The average refractive index is calculated using the formula $n_{\mathrm{avg}} = [\phi n_{\mathrm{solid}} + (1\text{-}\phi)n_{\mathrm{void}}]$, where ϕ is the solid volume fraction and n_{solid} and n_{void} are the refractive indices of the solid and void materials, respectively (ϕ is generally around 0.74 for a fcc colloidal crystal lattice and typically varies between 0.1 and 0.26 for inverse opal structures). The PMMA colloidal crystal films, and their inverse opal ceria replicas, show a fcc arrangement of spheres, with their fcc (111) planes parallel to the underlying glass substrate (Figure 1). In the case of first-order Bragg diffraction from fcc (111) planes, $d_{111} = 0.8165\ D$, where D is the average center-to-center distance

Table 1. Physical Properties of Inverse Opal Ceria and Reference Ceria Powders[a]

	calcination conditions						
CeO_2 sample	temperature (°C)	time (h)	lattice parameter, *a* (Å)	crystallite diameter, *L* (nm)	surface area (m^2g^{-1})	cumulative pore volume ($cm^3\ g^{-1}$)	average pore diameter (nm)
inverse opal	400	2 - as prepared	5.419	9.4	51.0	0.124	9.7
	800	4	5.410 (−0.2%)	38.3 (+407%)	18.2 (−64%)	0.057 (−54%)	12.5 (+29%)
nanoparticles (Prep 1)	400	2 - as prepared	5.415	12.9	74.5	0.232	17.7
	800	4	5.411 (−0.1%)	30.5 (+236%)	17.9 (−76%)	0.142 (−39%)	28.3 (+60%)
nanoparticles (Prep 2)	400	2 - as prepared	5.415	13.5	32.9	0.025	9.3
	800	4	5.410 (−0.1%)	40.3 (+298%)	2.4 (−93%)	0.013 (−48%)	28.9 (+310%)
powder <5 μm (Aldrich)	400	2	5.410		2.5	0.011	18.6
	800	4	5.410 (0%)		2.3 (−8%)	0.011 (0%)	18.6 (0%)

[a] Percent change in each parameter after calcination at 800 °C for 4 h is given in parentheses.

between spheres on the (111) planes. Thus, eq 1 simplifies to give

$$\lambda_{\max} = 1.633D\sqrt{{n_{\mathrm{avg}}}^2 - \sin^2\theta} \qquad (2)$$

Equation 2 indicates that by varying D, n_{avg}, or θ, we can change the wavelengths of light allowed to propagate through *fcc* photonic crystals. Experimentally, D and n_{avg} are determined by measuring the position of the reflectance maximum ($\lambda_{\max}$) at different angles of incidence, and plotting $\lambda^2_{\max}$ against $\sin^2\theta$. If Bragg diffraction conditions are satisfied, a straight line will result with slope $= -(1.633)^2D^2$ and y-axis intercept $= (1.633)^2D^2{n_{\mathrm{avg}}}^2$. From the experimentally determined n_{avg}, the solid volume fraction ϕ can be calculated.

Figure 4 shows UV–vis transmittance spectra collected from a PMMA colloidal crystal thin film in air at different angles of incidence ($\theta = 0$–25°) with respect to the surface normal of the (111) plane. At normal incidence ($\theta = 0°$), an intense stop band (transmittance minimum) is observed at 877 nm, arising from first order Bragg diffraction from (111) planes of the PMMA colloidal crystal. The normalized width of the PBG, calculated by dividing the fwhm of the PBG peak ($\Delta\lambda$) by the position of the PBG peak ($\lambda_{\max}$), was 0.086. Fabry–Perot oscillations are observed on the high wavelength side of the (111) stop band.[46] From the spacing of the oscillations, a PMMA colloidal crystal film thickness of around 10 μm was determined (approximately 30 layers of PMMA spheres). Other bands, with wavelength ratios with respect to the (111) stop band position of 0.483, 0.500, 0.522, 0.556, were also observed in the low wavelength region (400–500 nm, not shown) and caused by optical diffraction of light by the PMMA colloidal crystal.[11] In agreement with eq 2, the position of the PBG for diffraction from fcc(111) planes shifted to shorter wavelengths as the incident angle (θ) of light increased.

Figure 5 shows a plot of $\lambda^2_{\max}$versus $\sin^2\theta$ for the PMMA colloidal crystal. The data clearly obeys the modified Bragg's law expression given in eq 2. From the analysis, a center-to-center distance (D) between spheres on the individual (111) planes of 398 nm was determined, identical to that estimated from the SEM image of Figure 1b. The average refractive index of the colloidal crystal was 1.350, and thus the volume fraction (ϕ) of PMMA spheres in the structure is 71% (since $n_{\mathrm{PMMA}} = 1.492$). The value of 71% is close to the theoretical value of 74% expected for a fcc arrangement of solid spheres. The small difference between the experimental and theoretical values is readily explained by the necking of the PMMA spheres, which acts to increase the void volume fraction in the colloidal crystal.

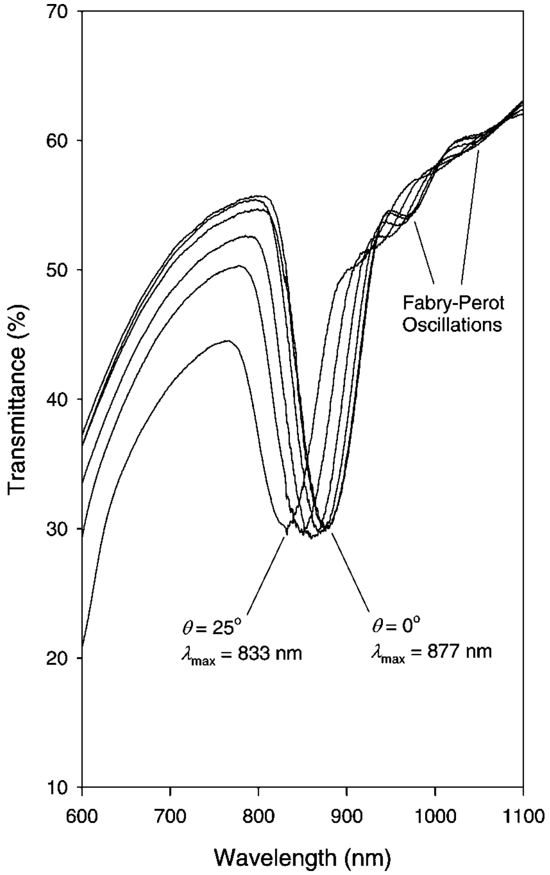

Figure 4. UV–vis transmittance spectra collected at different angles of incidence from a PMMA colloidal crystal film with $D = 398$ nm, where D is the center-to-center distance between spheres on *fcc* (111) planes. Angles of incidence were measured with respect to the surface normal of the (111) planes. At normal incidence ($\theta = 0°$), the colloidal crystal exhibits a PBG at 877 nm due to Bragg diffraction on fcc (111) planes. The position of the PBG shifted progressively to shorter wavelengths as the angle of incidence increased (the spectra were taken consecutively with 5° increments).

Angle-resolved UV–vis transmittance spectra collected in air from a CeO_2 inverse opal thin film are shown in Figure 6. At normal incidence ($\theta = 0°$), the inverse opal exhibited a PBG at 485 nm, which we assign to first order Bragg diffraction from the (111) planes of the fcc inverse opal structure. The normalized band gap width ($\Delta\lambda/\lambda_{\max}$) is 0.163, approximately twice that observed for the PMMA template

---

(46) Jiang, P.; Bertone, J. F.; Hwang, K. S.; Colvin, V. L. *Chem. Mater.* **1999**, *11*, 2132–2140.

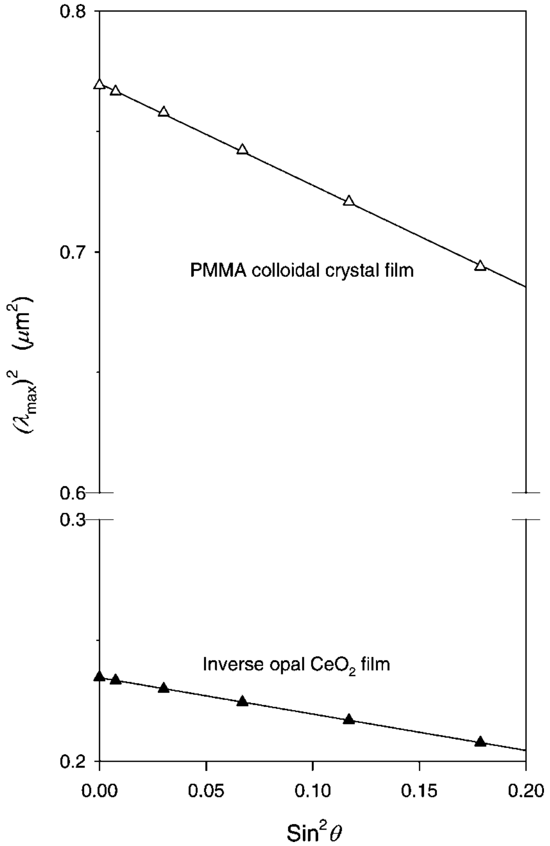

Figure 5. Plot of λ^2_{max} versus $\sin^2\theta$ for a PMMA colloidal crystal film and an inverse opal ceria film, where λ_{max} is the PBG position for diffraction from fcc (111) planes and θ is the angle of incidence with respect to the surface normal of the (111) plane. A linear-least-squares fit has been applied to each data set. From eq 2, it can be shown that the slope of the lines = $-1.633^2D^2$and the y-axis intercept = $1.633^2D^2{n_{avg}}^2$.

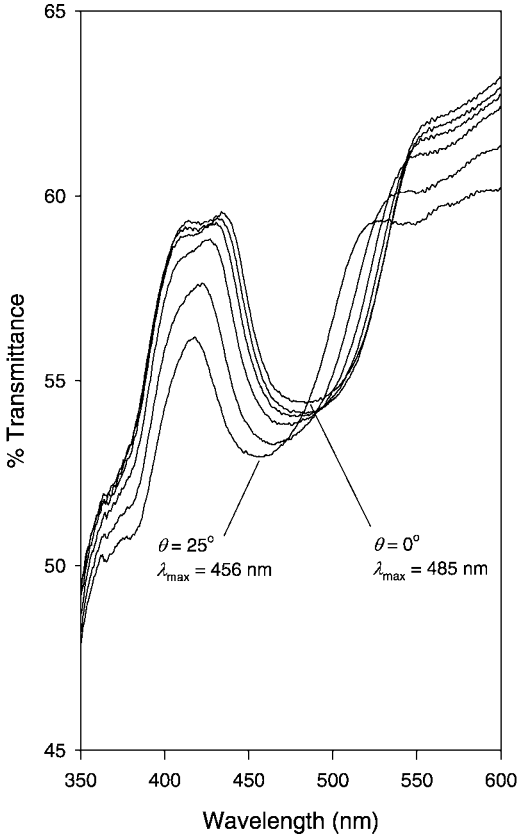

Figure 6. UV–vis transmittance spectra collected at different angles of incidence from an inverse opal CeO₂ film with D = 238 nm, where D is the center-to-center distance between spheres on fcc (111) planes. Angles of incidence were measured with respect to the surface normal of the (111) planes. At normal incidence (θ = 0°), the inverse opal exhibits a PBG at 485 nm due to Bragg diffraction on fcc (111) planes. The position of the PBG shifted progressively to shorter wavelengths as the angle of incidence increased (the spectra were taken consecutively with 5° increments).

($\Delta\lambda/\lambda_{max}$ = 0.086). In agreement with eq 2, the position of λ_{max} shifted to shorter wavelengths as the incident angle of light increased from 0 to 25°. Following the procedure above, we plotted λ^2_{max} vs $\sin^2\theta$ and achieved a straight line fit (Figure 5). From the plot, a D value of 238 nm and n_{avg} of 1.249 were obtained. Bulk ceria has a refractive index of 2.4,[45] so the ceria volume fraction in the inverse opal is 17.8%. The D value and ceria volume fraction determined from the UV–vis transmittance measurements are in good agreement with those estimated from the SEM micrographs of Figure 1c and d, demonstrating the close association between the geometric and optical properties of inverse opal. The UV–vis transmittance data confirms a 40% reduction in the value of D between the PMMA colloidal crystal template (D = 398 nm) and the CeO₂ inverse opal (D = 238 nm).

Refractive Index Sensing Using Inverse Opal CeO₂ Thin Films. Inverse opal materials are demonstrating potential for sensing applications,[25–27] because of their inherent optical properties and macroporosity. Refractive index sensing has been the subject of several recent works,[26,27] the basis of which can readily be understood using the following rationale. At normal incidence (θ = 0°), eq 2 reduces to

$$\lambda_{max} = 1.633Dn_{avg} \tag{3}$$

For a ceria inverse opal, $n_{avg} = [\phi n_{ceria} + (1\text{-}\phi)n_{void}]$. By filling the macropores (voids) in a ceria inverse opal with solvents of different refractive index, the position of the PBG for diffraction from fcc (111) planes is predicted to shift according to the relation

$$\lambda_{max} = 1.633D[\phi n_{ceria} + (1-\phi)n_{solvent}] \tag{4}$$

A plot of λ_{max} versus $n_{solvent}$ should thus yield a straight line with slope = $1.633D(1\text{-}\phi)$ and y-axis intercept = $1.633D\phi n_{ceria}$.

To test the viability of inverse opal ceria films for refractive index sensing applications, we collected UV–vis transmittance spectra at 20 °C and θ = 0° from an inverse opal CeO₂ film in air (n = 1.000), methanol (n = 1.329), acetone (n = 1.359), ethanol (n = 1.360), n-heptane (n = 1.387), dichloromethane (n = 1.424), carbon tetrachloride (n = 1.460), benzene (n = 1.501), 1,2-dibromoethane (n = 1.539), and 1,2,4-trichlorobenzene (n = 1.571), respectively. The spectra are shown in Figure 7. The PBG position shifted progressively to longer wavelength as the refractive index of the solvent on filling the macropores increased, in excellent agreement with theory (equation 4). The intensity of the stop band decreased with increasing $n_{solvent}$, reflecting the progressive decrease in the dielectric contrast between the CeO₂ and solvent. It should be noted that when $n_{solvent} = n_{ceria}$ = 2.4, no peak for diffraction from fcc (111) planes will be observed (i.e., the material will no longer behave as a photonic crystal because of the absence of periodic refractive index modulation).

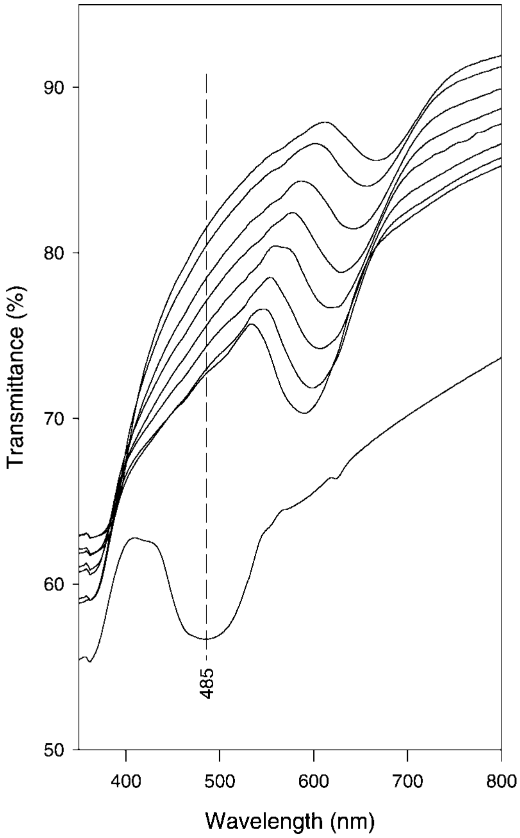

Figure 7. UV–vis transmittance spectra collected at normal incidence ($\theta = 0°$) from an inverse opal ceria film in air ($\lambda_{max} = 485$ nm) then solvents of increasing refractive index. Solvents used were methanol ($n = 1.329$), ethanol ($n = 1.360$), *n*-heptane ($n = 1.387$), dichloromethane ($n = 1.424$), carbon tetrachloride ($n = 1.460$), benzene ($n = 1.501$), 1,2-dibromoethane ($n = 1.539$), and 1,2,4-trichlorobenzene ($n = 1.571$). The vertical line at 485 nm was added to emphasize the shift in the position of the PBG (λ_{max}) with increasing $n_{solvent}$.

Figure 8 shows the position of the PBG (λ_{max}) in the spectra of Figure 7 as a function of solvent refractive index. An excellent linear least-squares fit is obtained ($r^2 = 1$), confirming the viability of inverse opal thin films for refractive index sensing applications. A sensitivity of $n = 0.001$ or better is achievable, based on the observed optical response of the inverse opal CeO_2 film to acetone ($n = 1.359$, $\lambda = 598.5$ nm) and ethanol ($n = 1.360$, $\lambda = 599$ nm). From the intercept and slope of the plot, the values $D = 238$ nm and $\phi = 17.8\%$ were extracted. These values are identical to those determined from the angle resolved UV–vis spectra of Figure 6.

In future work, we plan to investigate the performance of inverse opal CeO_2 powders as support materials for noble metal water–gas shift and reforming catalysts.

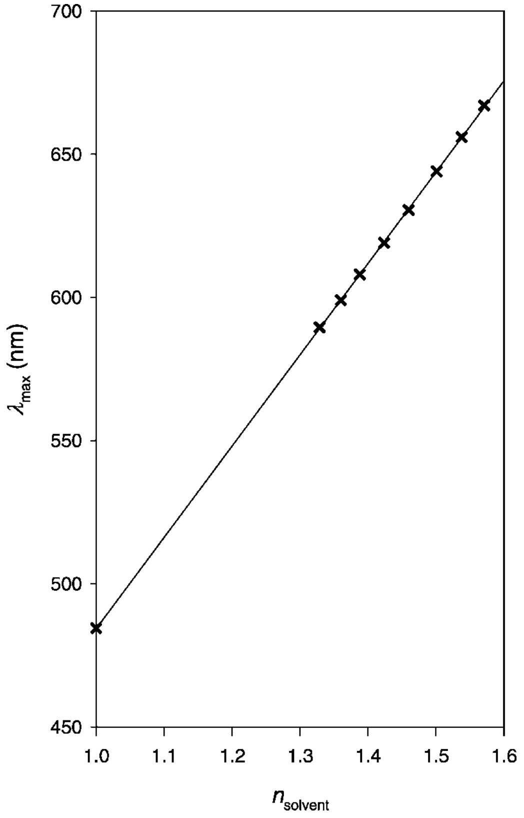

Figure 8. Plot of λ_{max} versus $n_{solvent}$ for a ceria inverse opal film. λ_{max} values were taken from the UV–vis transmittance spectra of Figure 7. The plot shows that the position of the PBG for diffraction on fcc (111) planes increases linearly with $n_{solvent}$, as predicted by eq 4.

Conclusions

Colloidal crystal templating is a simple and inexpensive method for the fabrication of inverse opal CeO_2 films and powders. CeO_2 inverse opals have intrinsically interesting physical and optical properties (such as 3DOM structures, nanometer size ceria crystallites, high surface area, high sintering resistance, and photonic band gaps) that may be exploited in various applications, in particular optical sensors and heterogeneous catalysis. Refractive index sensing with high sensitivity ($n = 0.001$ or better) is possible using inverse opal ceria thin films.

Acknowledgment. G.I.N.W. thanks the Foundation for Research Science and Technology for the award of a New Zealand Science and Technology Postdoctoral Fellowship (Contract UOAX0412).

CM703005G